ARTICLE

Check for updates

Fluctuation X-ray diffraction reveals three-dimensional nanostructure and disorder in self-assembled lipid phases

Andrew V. Martin [1][✉], Alexander Kozlov [2], Peter Berntsen [3], Francisco Gian Roque[3], Leonie Flueckiger[3], Saumitra Saha[2], Tamar L. Greaves[1], Charlotte E. Conn[1], Adrian M. Hawley[4], Timothy M. Ryan[4], Brian Abbey [3] & Connie Darmanin [3][✉]

Emergent nanoscale order in materials such as self-assembled lipid phases, colloidal materials and metal-organic frameworks is often characterized by small-angle X-ray scattering (SAXS). Frequently, residual disorder in these materials prevents high-resolution 3D structural characterization. Here we demonstrate that angular intensity variations in SAXS patterns can provide previously inaccessible information about local 3D structure via a rich, real-space distribution of three- and four-body statistics. We present the many-body characterisation of a monoolein-based hexagonal phase doped with a phospholipid, revealing non-uniform curvature in the lipid channels, likely due to phase separation of the lipids in the membrane. Our many-body technique has general applicability to nanomaterials with order in the range $10\,nm^{-1}\,\mu m$ currently targeted by synchrotron SAXS and has the potential to impact diverse research areas within chemistry, biology and materials science.

[1] School of Science, RMIT University, Melbourne, VIC 3000, Australia. [2] Australian Research Council Centre of Excellence in Advanced Molecular Imaging, School of Physics, The University of Melbourne, Melbourne, VIC 3010, Australia. [3] Australian Research Council Centre of Excellence in Advanced Molecular Imaging, Department of Chemistry and Physics, La Trobe Institute for Molecular Science, La Trobe University, Melbourne, VIC 3086, Australia. [4] Australian Synchrotron, Clayton, Melbourne, VIC 3168, Australia. [✉]email: andrew.martin@rmit.edu.au; c.darmanin@latrobe.edu.au

M aterials with emergent nanoscale order, such as self-assembled lipid phases[1], metal-organic frameworks[2] and colloidal materials[3] are ubiquitous in the search for technological innovations in health, energy, optics and electronics. However, their emergent order is rarely perfect or well-understood. The design and discovery of these materials is impacted by residual nanoscale structural disorder that is difficult to characterize. In biological lipid membranes this disorder manifests as phase separation, heterogeneity and bilayer asymmetry in the membrane composition and all these impact the function of biological cells[4], drug delivery[5] and membrane protein crystallization[1]. In studies of metal-organic frameworks, there is a growing appreciation that disorder in the form of flexibility, defects and long-range disorder is the rule, rather than the exception[2].

Nanoscale order is commonly characterized using small-angle X-ray scattering (SAXS) which can reveal the types of local crystalline packing and quantifies local length scales, such as the lattice parameter. SAXS measurements record diffraction from an ensemble of randomly oriented local structures. Their random orientation leads to isotropy in 2D SAXS diffraction data with respect to rotation around the beam axis. The effectively 1D SAXS intensity data can be mapped into a real-space distribution of pair distances (pair or radial distribution function)[6]. A fundamental limitation of SAXS is that the pair distribution function lacks information about local angles and orientation in the atomic or molecular structure.

When the number of exposed crystal domains (or local structures) is small, however, the 2D SAXS diffraction is not isotropic with respect to rotation around the beam axis. For example, the diffraction rings of self-assembled lipid phases can appear textured, spotty or broken as shown in Fig. 1a and b. The angular intensity variations contain 3D structural information that is targeted by emerging X-ray fluctuation diffraction techniques such as X-ray cross-correlation analysis[7–9], largely inspired by the pioneering work of Kam in the 1970s on the fluctuations of small-angle protein scattering[10]. These methods study intensity correlations of pairs of pixels on the detector as a function of scattering vector magnitude and angular separation averaged over a large number of independent measurements. Although Kam's proposal to determine macromolecular structure from solution was not realised for proteins due to radiation damage and noise limitations, there has been renewed interest that these problems can be overcome with X-ray free-electron laser sources. In recent years, intensity correlation methods have been developed for imaging single particles[8,11,12] and extended to disordered systems such as colloids[7,13] and liquid crystals[9]. They have also been developed for electron diffraction to study metallic glasses and amorphous solids[14].

The structural interpretation of fluctuation X-ray scattering of bulk disordered materials is elusive because intensity correlations encode 3D structural information indirectly. For example, the identification of local angular symmetries can be obscured in q-space correlations by the density of local scatterers, as observed in simulation studies[15]. The X-ray scattering of structural models must be forward simulated to compare to q-space intensity calculations and it is not always obvious how to improve models to rectify discrepancies between simulation and experiment. To address this limitation, we have proposed that the intensity correlation data can be converted into a three- and four-body real space distribution[16] that we call the pair-angle distribution function (PADF) (see Fig. 1c). The PADF generalizes the pair-distribution $g_2(r)$ accessible by conventional electron or X-ray scattering methods to higher dimension and it contains information about local angular structure that is missing in pair statistics. The PADF is three-dimensional (two pair distance

coordinates and an angle coordinate) and takes the form

$$\Theta(r, r', \theta) = \tilde{g}_2(r, r' = r, 0) + \tilde{g}_3(r, r', \theta) \\ + \tilde{g}_3(r, r', \pi + \theta) + \tilde{g}_4(r, r', \theta), \quad (1)$$
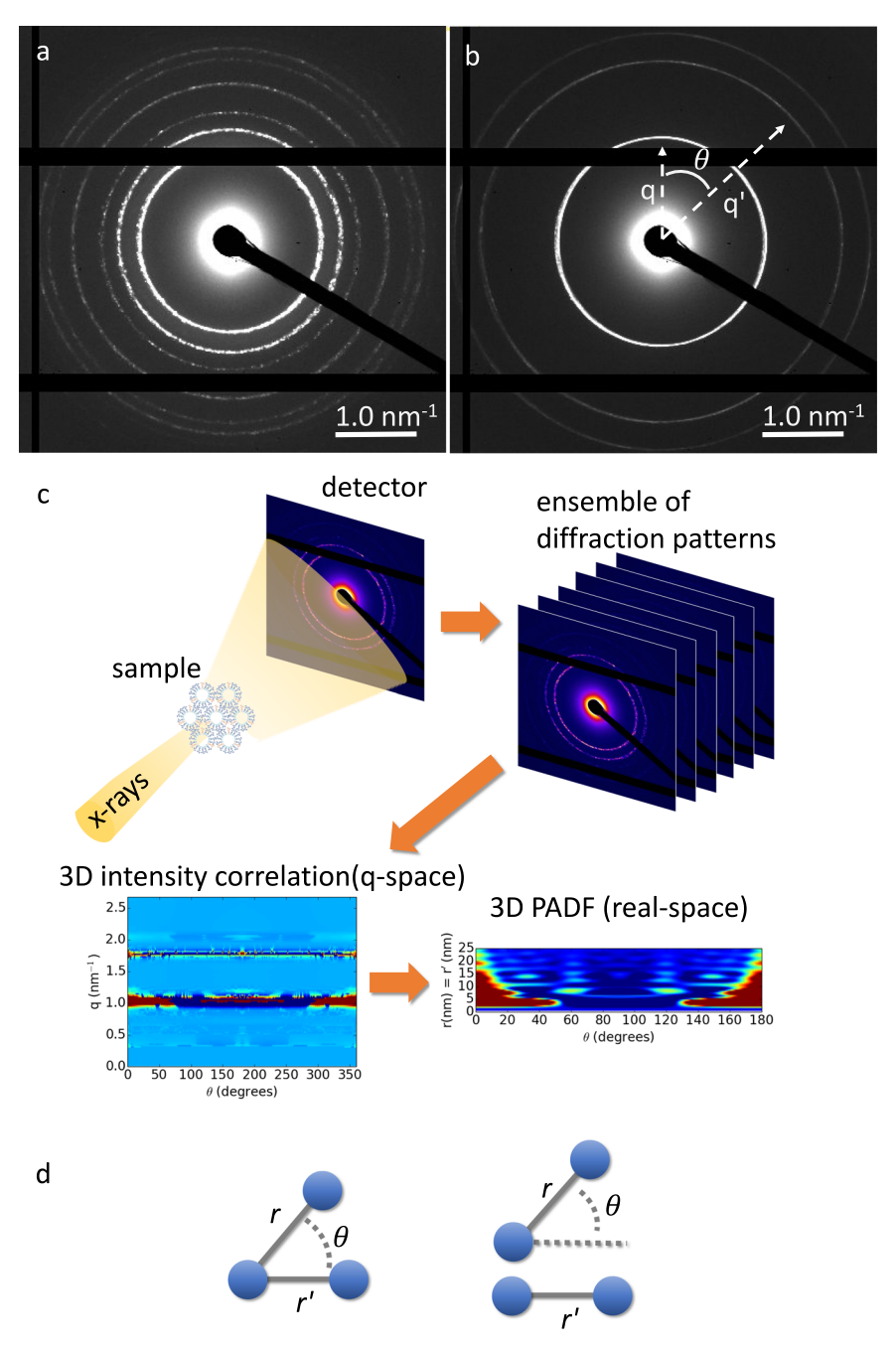
where coordinate definitions are shown in Fig. 1d. The tilde notation $\tilde{g}$ indicates that these terms are modified from the standard correlation function g_n of statistical mechanics (see Supplementary Methods S1). The PADF contains peaks associated with favoured atomic arrangements and the angular peak positions can be directly interpreted with simple geometric models. The relationship we have found between the PADF and the fluctuation diffraction data requires that the local structures or crystal domains have no preferred orientation with respect to the beam axis, which is further discussed in Supplementary Methods S1. As an ensemble distribution, the PADF is applicable even when the crystal domains are disordered due to the presence of, for example, strain, stress or defects. Note the second three-body term in Eq. (1) mirrors the angular distribution around 90 degrees and the four-body term contains the same symmetry. The PADF analysis accounts for Ewald sphere curvature and the PADF symmetry persists even at high scattering angles where diffraction centrosymmetry is broken by Ewald sphere curvature.

Here we present a demonstration of a PADF measurement with X-rays to observe details of the nanoscale organization of self-assembled membranes not accessible to conventional SAXS experiments. Self-assembly membranes were chosen to demonstrate the impact of PADF as they produce a textured 2D pattern under certain conditions which is a requirement for PADF analysis. For this reason, we study the changes in the many-body real-space distribution of a monoolein(MO):buffer mixture (see 'Methods' for buffer composition), relevant for membrane protein crystallization, as it undergoes a transformation from cubic to a hexagonal phase. In these phases, the lipid membranes form cylindrical channels that enclose the solvent and stack into a 2D lattice with hexagonal symmetry or a 3D network with cubic symmetry. The phase change is induced via the addition of cholesterol and 1,2-dioleoyl-phosphatidylcholine (DOPC). These additives are used in protein crystallization trials to find conditions conducive to crystallization. One can envision using the PADF in the future to gain further structural insight into favourable protein crystallization conditions, to determine the molecular mechanisms underpinning membrane protein crystallization in liquid crystal phases, to study membrane-protein interactions, structural ordering of drugs within colloidal materials and possibly to help further our understanding of the self-assembly material in batteries. To realise these applications, we must first understand the structural sensitivity of the PADF for self-assembled phases without protein, which we address here. Both the cubic and hexagonal phases produce PADF distributions rich in information, which made this system an ideal target for demonstrating the capabilities of the PADF technique.

Results

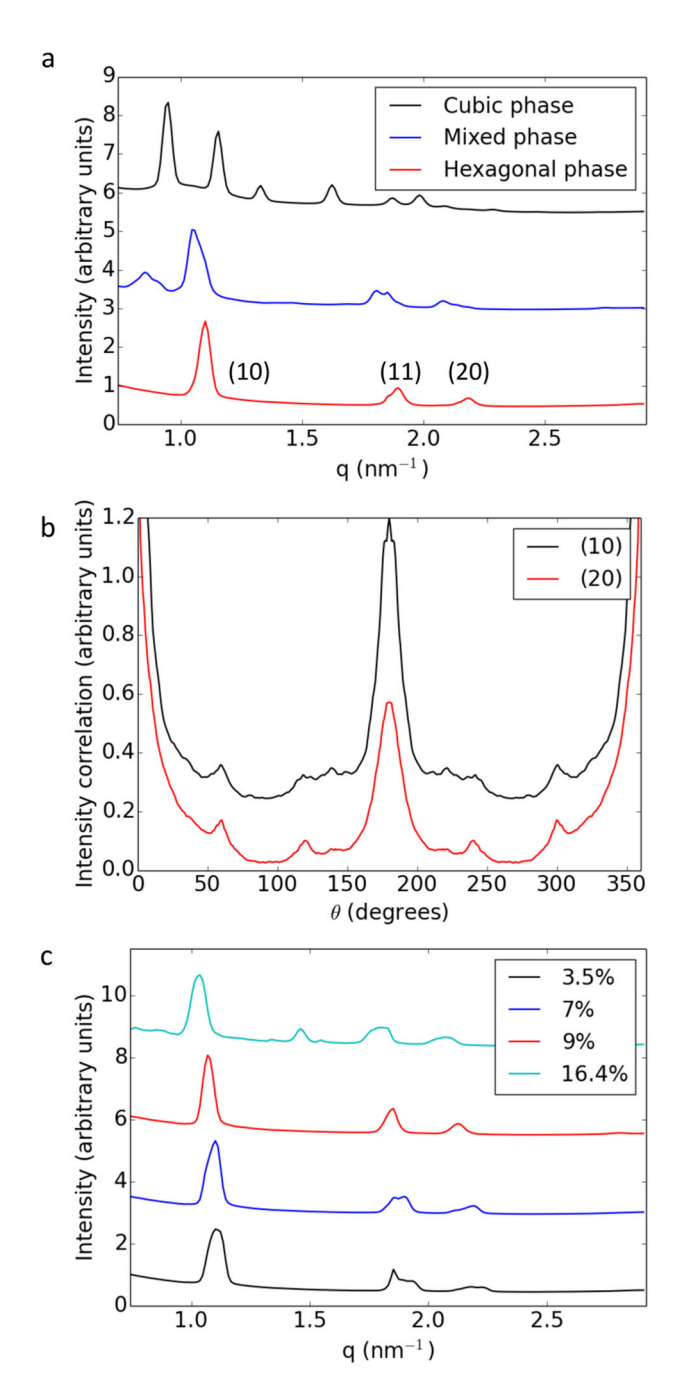**Fluctuation X-ray scattering experiment.** Fluctuation X-ray scattering data were collected at the SAXS/WAXS beamline of the ANSTO Australian Synchrotron. Figure 1a, b shows the diffraction from cubic and hexagonal phases exhibiting angular intensity variations in the diffraction rings which contain the structural information required to measure the PADF. We measured monoolein:protein buffer mixtures doped with cholesterol and DOPC. The cholesterol concentration was 3.7% (w/w) and six DOPC concentrations were measured from 0–16.4% (w/w). These dopants and concentrations are relevant for the potential crystallization studies of dopamine receptors[17]. Every sub-well of a 96-well crystallization plate was prepared with droplets of a

Fig. 1 Experiment setup and PADF coordinates. a The diffraction pattern of a MO:buffer mixture in the Pn3m cubic phase and **b** the diffraction pattern of MO:buffer doped with 3.7% cholesterol and 9% DOPC in the hexagonal phase. To improve visibility of the angular variations in outer rings, both **a**, **b** are displayed with a linear intensity scale with a maximum intensity displayed set lower than the maximum intensity recorded. There are large angular variations relative to the average intensity in all rings in both phases. **c** The sample is scanned relative to the X-ray beam to measure an ensemble of diffraction patterns. From the ensemble a 3D q-space intensity correlation function is generated. The intensity correlation is transformed into the 3D real-space PADF. **d** The PADF is a function of pair distances and an internal angle. In the three-body case, the two pairs share a common atom. In the four body case, the two pairs are distinct.
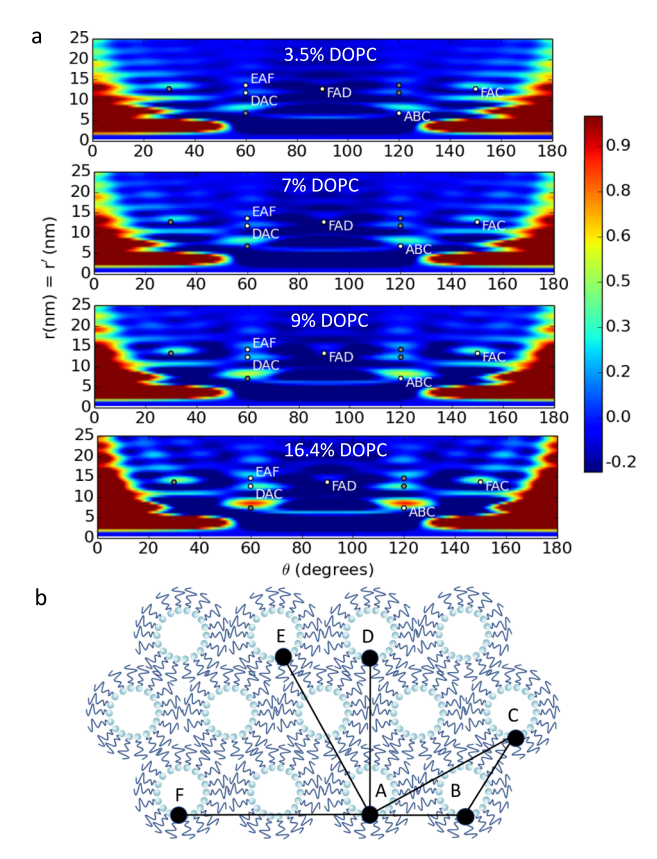
single sample condition, providing a total of 192 sub-wells which were included in our analysis. By raster scanning a plate with respect to the X-ray beam, we were able to collect 16 diffraction patterns per drop for a total of around 3000 diffraction patterns per sample condition. All sample conditions were observed to form either the hexagonal phase, diamond cubic (Pn3m) phase or a mixture of the two phases (see Fig. 2a). Salts, such as those in the protein buffer, are known to favour transitions to the hexagonal phase[18], rather than a transition to the lamellar phase as is typically observed when DOPC is added to MO:water[19,20]. Cubic

and hexagonal phases were deliberately targeted in this experiment to produce angular structure for the PADF analysis, as shown by angular peaks that appear in the intensity correlation function (Fig. 2b). A spectral clustering method (see 'Methods' and Supplementary Methods S2) was applied to the 1D powder radial intensity data to identify subsets of data with a consistent lipidic phase (refer to Supplementary Methods S3, Supplementary Table 1, Supplementary Figs. 1 and 2 for more details). At 0% DOPC concentration we observed a dominant diamond cubic phase and for DOPC concentrations greater than 4% we observed

Fig. 2 Cubic and hexagonal phases. a Example SAXS radial intensity plot of cubic, hexagonal and mixed phases recovered after clustering and averaging the data. Intensity is plotted on a log scale. Note the mixed phase may originate from phase co-existence and/or data clustering. The hexagonal peaks are labelled by Miller indices in 2D, because the hexagonal lattice is periodic in 2D and extended in the third dimension. **b** The angular correlations of the hexagonal phase (10) and (20) rings for MO:buffer doped with 3.7% cholesterol and 9% DOPC. **c** Radial intensity plots from the data identified to be purely hexagonal phase for a MO:buffer:cholesterol mixture as a function of added DOPC concentration. Intensity is plotted on a log scale.

Fig. 3 Real-space angular structure of the hexagonal phase. a 2D cross-sections of the $r = r'$ plane of the PADF as a function of DOPC concentration. The white markers correspond to the three-body peaks indicated in (**b**) and grey markers are the symmetry partners. The marker labels are defined in part (**b**) of the figure. There is a significant increase in the amplitude of angular correlation peaks around the 60 (120) degrees that are strongly associated with an ordered hexagonal lattice. The maximum and minimum values on the colour scale were set to enhance contrast of the most relevant peaks. All images are on the same absolute, linear scale. **b** Diagram of indicative points in a hexagonal lattice that give rise to the peaks observed in the data. Hexagonal phases with higher percentages of DOPC display peak positions in better agreement with an ideal hexagonal lattice than those with low percentage of DOPC.

For this reason the angular correlations were not analysed at this composition.

For each diffraction pattern the intensity correlation function was calculated (see Fig. 1 and 'Methods') and averaged over the ensemble of data. Corrections for backgrounds, detector gaps and masked pixels are described in the Supplementary Methods S4. The large number of measurements (>500) is needed to ensure that on average we have measured crystals in all orientations and that the correlation function has converged. If the sample has disorder, the dataset is averaged over the ensemble of disordered structures and assumed to converge to the mean distribution for the bulk material. A series of linear transformations (see Supplementary Methods S4 and ref. [16]) is performed to map the correlation function into the PADF described by Eq. (1).

Hexagonal phase results. The 1D SAXS curves for the hexagonal phase as a function of DOPC concentration are shown in Fig. 2c. It shows a minor shift in the lattice parameter (see Supplementary Methods S2, Supplementary Table 2) and some splitting of the (11) peak, but otherwise the phase is consistent through the series. Figure 3a shows the $r = r'$ cross-section of the PADF as a

a dominant hexagonal phase. Data from non-dominant phases or mixed phases comprised only a small percentage of each dataset and was excluded from the PADF analysis. At 2% DOPC the system is close to the cubic:hexagonal phase boundary and the proportion of these phases varied among the different droplets.
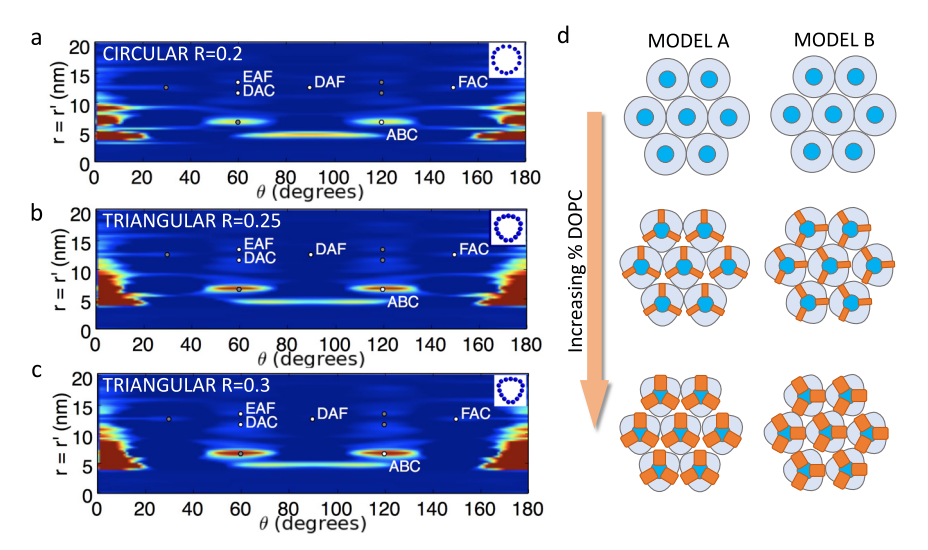
Fig. 4 Geometric models of the hexagonal phase. Calculations of three- and four-body arrangements present in a 2D hexagonal lattice with increasing radius of curvature. The model is created by positioning points on the interior edge of the channel (see Supplementary Methods S5 for further details). The white markers indicate peak locations from the three-body terms present in an ideal hexagonal lattice as defined in Fig. 3b and grey markers are their symmetry peaks. The channel shape is shown as inset in the top right corner in (**a**–**c**). **a** Circular channels with radius of curvature of 0.2 (fractional coordinates). **b** Triangular channels with curved sides with a radius of curvature of 0.25 (fractional coordinates). The orientation of the channel aligns with the hexagonal lattice. **b** Triangular channels with curved sides with a radius of curvature of 0.3 (fractional coordinates). **d** Two models of the DOPC distribution that could give rise to the geometric triangular model. DOPC-rich regions are indicated in orange.

function of dopant concentration. The angular peaks around 60 and 120 degrees are characteristic of the hexagonal lattice as shown by the geometric model in Fig. 3b. Note the PADF contains a mirror symmetry around 90 degrees and does not discriminate between peaks located at 60 and 120 degrees.

Strikingly, the amplitude of the 60 (120) degree peaks grow steadily when the DOPC concentration is increased from 3.5 wt% to 16 wt%. A removal of strain or polydispersity of channel size cannot explain the amplitude change, because both these effects cause deviations in angular peak positions that are not observed in this concentration range. Furthermore, it cannot be explained by only an increase in domain size of crystalline regions because an increase in the number of otherwise ordered unit cells would lead to a simple scaling of the PADF intensities. Instead we observe non-uniform changes with angular PADF coordinate θ.

Hexagonal phases contain a packing frustration energy related to voids that form in cylinder packing[21]. Voids are prevented by either non-uniform tail length or non-uniform membrane curvature. As MO and DOPC both contain an oleoyl chain of similar length, it is unlikely that void formation can be avoided by the variation in the MO and DOPC chain lengths or chain positions relative to the lipid-solvent interface. DOPC is also known to decrease the curvature of monoolein membranes[22], which motivates exploring the impact of channel curvature on the angular peak structure. We have found that a model of a triangular distortion that gradually modifies the curvature on three faces can reproduce a similar trend in the data as shown in Fig. 4a–c. Gradually increasing the curvature of a triangular distortion causes the hexagonal peaks to increase in amplitude, while angular structure near 30 degrees and 90 degrees is suppressed. At the same time, the curvature change does not greatly impact the peak ratios in the 1D SAXS radial intensity data, consistent with the experimental data. These trends are only reproduced when the triangular shaped channels are oriented in alignment with the hexagonal lattice.

The molecular explanation of the triangular channel shape can be built on previous knowledge of how DOPC behaves in monoolein membranes. First, it requires that membrane composition separates into DOPC rich locations and DOPC depleted locations. Although there is not a specific observation of DOPC:MO separation in the hexagonal phase to our knowledge, phase separation is commonly observed in membranes of lipid mixtures and correlated with non-uniform curvature[23]. Heterogeneous lipid distribution and curvature are also an integral part of biological membranes[4]. The DOPC-rich regions are known to reduce the local curvature of the membrane[22]. We have developed two models of the spatial distribution of the DOPC-rich regions that give rise to a triangular shape. Both models explain the angular PADF peak positions and the trend in the PADF data equally well. In Model A (see Fig. 4d), the DOPC-rich regions are located at gaps between channels. There are two types of gaps: those bordered by three DOPC-rich membrane sections and those bordered by three DOPC-depleted membrane sections. The second model, Model B, positions the DOPC-rich regions at the contact points with three neighbouring channels to form a three-fold symmetry. In Model B, there is also a lipid asymmetry with DOPC enriched on only one side of the contact point. Asymmetry is also common in biological membranes[4]. In both Models A and B, the distorted channel shape can be periodically repeated with close to the same lattice spacing as the 0% DOPC lattice.

Cubic phase results. We further studied the PADF of monoolein: buffer mixture in the cubic Pn3m phase with and without cholesterol. The 1D radial intensity curves are shown in Fig. 5a. The sample with cholesterol shows a swelling of the lattice, but otherwise a similar SAXS intensity profile to the sample without cholesterol. Fig. 5b shows the $r = r'$ cross-section of the PADF for the cubic phases and demonstrates significant angular changes when cholesterol is added. There are distinct changes in the angular peak structure of the PADF near both 60° and 90° in the range $10 < r < 20$ nm. A simple geometric model of channels with Pn3m symmetry reproduces 60° and 90° PADF peaks consistent with the observed positions of the sample with cholesterol (see Fig. 5c and d). The low-angle peaks (<60°) in the PADF data are likely due to the membrane structure that fills the space between
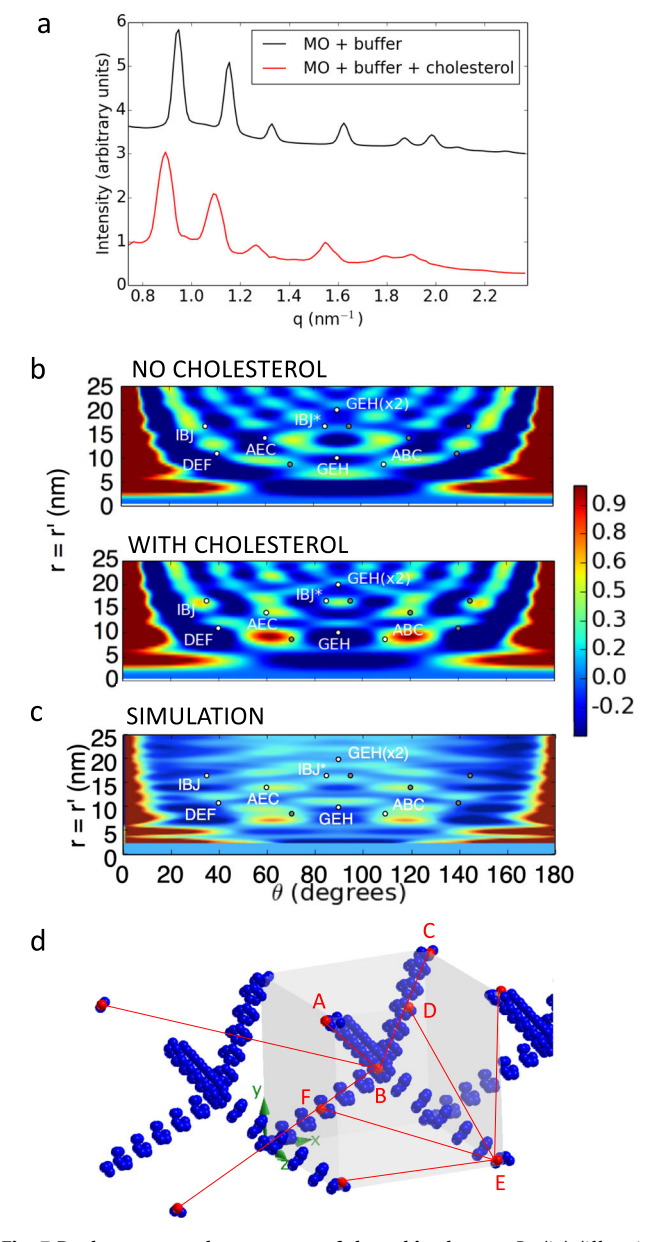
the channels, which are not included in the model. In the case where no cholesterol is present, the peak positions are shifted away from those predicted by the simple channel model. These results indicate that cholesterol does more than just swell the unit cell, it also modifies the lattice disorder and/or the channel geometry within each cell. Cholesterol is known to increase the stiffness of the monoolein membranes, which is expected to increase order and make the lattice more rigid[22]. This may account for the improved agreement between observed and simulated angular peak positions when cholesterol is added.

Discussion

The key difference between a conventional SAXS experiment and a fluctuation SAXS experiment is the amount of data collected. The amount of data required depends on a number of factors including resolution, sample heterogeneity and the beam intensity. In this experiment, the cubic phase was deliberately targeted because it contained sufficiently large crystal domain sizes, producing intensity variations with polar angle that are visually identifiable and much larger than noise levels. There are >10^3 crystal domains per exposure ensuring that a sufficient number of lattice orientations are sampled in the dataset. Self-assembled lipid phases can be insightfully analysed at low resolution which helps to minimise the amount of data required. Our experiment confirms for samples with a crystalline local order and a lattice spacing of the order of 10 nm, a dataset of order of 10^3 patterns is sufficient. Aside from self-assembled lipid materials, we expect other materials with emergent nanoscale order, such as colloidal materials and metal-organic frameworks, to meet these requirements. Our datsets of around 3000 patterns took around 1.5 h to measure and it is not unreasonable to increase the dataset size by 10 times for samples that exhibit greater heterogeneity of local structures. For materials with smaller crystal domain sizes, it may be advantageous to use microfocus or nanofocus synchrotron beams to ensure intensity fluctuations are not small relative to mean radial intensity in each diffraction ring.

The largest real-space distance and angular resolution is currently limited by statistics. Evaluating the PADF plots to larger real-space distances (>25 nm) show regions affected by noise. Evaluating at finer angular resolutions produces little change. In principle, both the largest real-space distance and the angular resolution are limited by detector size and the experimental geometry. However, this is not the case for our data and significantly larger datasets and/or higher signal-to-noise measurements would be required to reach the detector limits.

X-ray beam anisotropy can impact PADF measurements if length scales approaching the beam size are analysed. In our experiment, the lattice domain sizes (≈1 micron) are much smaller than the beam size (25 micron × 250 micron) and no effect of the beam anisotropy is observed in the diffraction spots. Additionally, we analyse real-space dimensions in the PADF of the order of 10 nm, where the impact of beam anisotropy is not observed.

The PADF is a rich, continuous 3D distribution and we are not yet able to model all the information it contains. Here we have focused on the information that is most readily interpreted, namely the angular peak positions and the trends that emerge with changes in sample composition. The angular peak positions show good agreement with geometric models, providing strong evidence that the promise of PADF theory[16] has been translated into experimental success. Trends with sample composition are more difficult to unambiguously interpret and require additional prior knowledge about diffraction physics and the sample. For example, in the case of increasing DOPC concentration we ruled out a change in lattice domain size as an exclusive explanation

Fig. 5 Real-space angular structure of the cubic phase. a Radial diffraction lineplots of the MO:buffer Pn3m lipidic cubic phase with and without cholesterol (3.7%) plotted on a log scale. Cholesterol induces an increase in the lattice parameter but otherwise radial profiles are similar. **b** 2D cross-sections of the $r = r'$ plane of the PADF for the same cubic samples with and without cholesterol. White markers are three-body terms predicted from the Pn3m model shown in (**d**) and black markers are their symmetry peaks. GEHx2 is the same geometry as GEH with the pair distances doubled. IBJ* is similar to IBJ, but with point J rotated 90 degrees around a lattice vector intersecting point B. The markers are reproduced on the experimental data to aid comparison. There are significant changes observed in the angular peak positions when cholesterol is added. The maximum and minimum values on the colour scale were set to enhance contrast of the most relevant peaks. Both experimental images are on the same absolute, linear scale. **c** Simulation of the angular distribution from a geometric Pn3m model with channels to compare to peak positions (but not the contrast) of the experimental results (see Supplementary Methods S5 for further details). **d** The Pn3m simulation model. To reduce computation time, each channel contains six rings of point scatterers.

due to the non-uniform angular dependence of the observed trends (for further evidence of this non-uniformity see Supplementary Discussion and Supplementary Figs. 3 and 4).

Beyond synchrotron applications, PADF analysis could potentially be used at X-ray free-electron laser facilities to probe atomic length scales to study bonding and short-range order in glasses and liquids. The scattering of atomically disordered materials is diffuse and produces a correlation function with significantly lower signal-to-noise. However, theory predicts that X-ray free-electron lasers could provide the intensity and high-throughput data collection to overcome the noise limitations and reach atomic resolution[16]. The femtosecond duration of XFEL pulses can also outrun the diffusion timescales of liquids and provide the time-resolution for dynamical studies of, for example, phase transitions.

Our results demonstrate that three- and four-body real-space distributions can be extracted from small-angle x-ray scattering of lipid materials with nanoscale order. This is experimental confirmation of the relationship between fluctuation X-ray scattering and multi-body real-space correlation functions previously only predicted theoretically[16]. The many-body distributions reveal local angular order inaccessible to conventional SAXS experiments and for lipidic materials and, specifically, we have shown the high sensitivity of the 3D real-space PADF characterization to small changes in lipid composition. Samples in the same phase identified by the 1D SAXS data show extensive differences in the PADF angular peak structure. Supported by simulation there is strong evidence that the angular peak structure reveals detail about the extent of lattice disorder (i.e. strain) and lipid channel shape. The increase in sensitivity to additive distributions and lattice disorder opens up exciting possibilities for the PADF technique to provide detailed structural characterization of dopants, proteins and drugs in lipid environments.

Notably, the PADF technique is based on an innovation of data analysis and does not require additional experimental equipment or unusual X-ray beam properties. The only modification to a standard SAXS experiment is to collect more data of a single sample composition. Hence, there should be few barriers to wide implementation of the PADF method with current synchrotron facilities with existing SAXS instruments. Based on the success with lipid materials, we expect that the 3D PADF analysis can be applied with similar success to other nanocrystalline materials with lattice parameters on the order of several nanometers, such as colloidal materials and metal-organic frameworks.

Methods

Materials. Monoolein (MO) and cholesterol were obtained from Sigma. DOPC was purchased from Avanti Polar Lipids (Alabama, USA). Milli-Q H_2O (18.2 MΩ cm) was used for sample preparations.

Sample preparation. Lipid mixtures were prepared and dispensed similar to the protocol outlined in Darmanin et al.[17]. Briefly, a stock of 200 mg/ml MO in ethanol, 20 mg/ml cholesterol in chloroform and 100 mg/ml DOPC in chloroform were made. These stocks were used to make a final MO mixture of 0.21 mg containing 3.7% (w/w) cholesterol and between 0 and 16.4% (w/w) DOPC. A total of 0.21 mg of lipid mixture was deposited onto a Swissci 96-well 2 drop crystallisation plate (Molecular Dimensions) using the Formulatrix NT8 robot. Each well was 2.8 mm diameter. The drops of mixture did not fill each well and were ~1–2 mm diameter. The plates were left overnight in the fume hood to evaporate off the solvent and then re-hydrated with either water or buffer (20 mM Bis-Tris Propane, 1 M NaCl, 10% glycerol, pH 7.7 and 0.8% PMAL-C12) to a final solvent content of 40% (v/w) and lipid content of 60% (v/w). Each sample composition was reproduced in one entire 96-well plate to obtain a total of 192 drops of the same lipid mixture for data analysis and to ensure reproducibility of the phase.

Data collection. The crystallisation plates were mounted directly on to the SAXS/WAXS beamline at the ANSTO Australian Synchrotron, which allowed in situ characterisation of the mesophases. The photon energy was 12 keV and the beam size was ~25 micron × 250 micron. The transmitted flux was 4×10^{12} photons s^{-1}

measured by a photodiode on the beamstop. The diffraction data were recorded on a Pilatus2-1M silicon photon counting detector (Dectris, Switzerland) with an exposure time of 0.5 s. The sample plate was scanned relative to the beam to measure 16 positions per droplet to acquire ~3000 diffraction patterns per plate. The large number of diffraction patterns were required for sufficient statistics for the correlation analysis.

The beam centre and detector distance was calibrated with the first diffraction ring of silver behanate and 1D radial plots were generated with Scatterbrain[24].

Radiation damage threshold were checked by 120 repeat measurements of a single sample position in 0.5 s exposures. Significant changes to the 1D SAXS intensity were only observed after several seconds.

A very small number of diffraction patterns of the hexagonal phase showed extremely bright Bragg peaks in the (10) ring that produced large errors in the PADF analysis. These patterns were removed by calculating a histogram from total integrated intensity on detector for the ensemble of data. Outliers with very bright total intensity were removed from the dataset prior to performing intensity correlation analysis.

Data classification. Peak positions in the 1D radial line plots were located using a continuous wavelet transform peak-finding algorithm implemented by SciPy as signal.find_peaks_cwt()[25].

The radial plots were clustered using spectral decomposition and k-means clustering adapted from ref. [26]. A similarity metric, d, for the spectral decomposition was constructed based on peak number and position as described in the Supplementary Methods S3. The phases of each cluster was manually identified and merged to produce a small number of clusters (3–5) each with a consistent phase as described in the Supplementary Methods S3.

Fluctuation analysis. The 3D q-space correlation functions required for PADF analysis are given by

$$C(q, q', \Delta\theta) = \int d\theta \langle I(q, \theta + \Delta\theta) I(q', \theta) \rangle_\alpha, \qquad (2)$$

where $I(q', \theta)$ is a 2D diffraction pattern expressed in polar coordinates (q, θ) and $\langle \rangle_\alpha$ is an average over an ensemble of measurements. These were calculated by first sampling each diffraction in polar coordinates (q, θ). The q-dimension was sampled linearly accounting for the Ewald sphere. The angular correlation was performed as a series of 1D convolutions in the θ dimension for each (q, q') coordinate. The processing of the correlation functions is described in Supplementary Methods S4. The angular correlation functions are converted into the PADF using the procedure outlined in ref. [16] and briefly described Supplementary Methods S4.

Data availability
The 2D SAXS diffraction patterns used to produce experimental results in Figs. 1–4 and 5 are publicly available. Data are available from the following Figshare repository: (10.25439/rmt.12253310)[27].

Code availability
Custom written code to analyse the data is available at https://github.com/amartinrmit/py2PADF.

References
1. Caffrey, M. A lipid's eye view of membrane protein crystallization in mesophases. *Curr. Opin. Struct. Biol.* **10**, 486–497 (2000).
2. Bennett, T. D., Cheetham, A. K., Fuchs, A. H. & Coudert, F.-X. Interplay between defects, disorder and flexibility in metal-organic frameworks. *Nat. Chem.* **9**, 11 (2016).
3. Xia, Y., Gates, B., Yin, Y. & Lu, Y. Monodispersed colloidal spheres: Old materials with new applications. *Adv. Mater.* **12**, 693–713 (2000).
4. Escribá, P. V. et al. Membranes: a meeting point for lipids, proteins and therapies. *J. Cell. Mol. Med.* **12**, 829–875 (2008).
5. Shah, J. C., Sadhale, Y. & Chilukuri, D. M. Cubic phase gels as drug delivery systems. *Adv. Drug Deliv. Rev.* **47**, 229–250 (2001).
6. Billinge, S. & Thorpe, M.F. (eds.). *Local Structure from Diffraction* (Kluwer Academic Publishers, 2002).
7. Wochner, P. et al. X-ray cross correlation analysis uncovers hidden local symmetries in disordered matter. *Proc. Natl Acad. Sci. USA* **106**, 11511–11514 (2009).
8. Kirian, R. Structure determination through correlated fluctuations in x-ray scattering. *J. Phys. B: At. Mol. Opt. Phys.* **45**, 223001 (2012).

9. Kurta, R. P., Altarelli, M. & Vartanyants, I. A. *Structural Analysis by X-ray Intensity Angular Cross-correlations*, 1–39 (John Wiley & Sons, Ltd, 2016).
10. Kam, Z. Determination of macromolecular structure in solution by spatial correlation of scattering fluctuations. *Macromolecules* **10**, 927–934 (1977).
11. Saldin, D. K. et al. Beyond small-angle x-ray scattering: Exploiting angular correlations. *Phys. Rev. B* **81**, 174105 (2010).
12. Starodub, D. et al. Single-particle structure determination by correlations of snapshot X-ray diffraction patterns. *Nat. Commun.* **3**, 1–7 (2012).
13. Liu, A. C. Y., Tabor, R. F., de Jonge, M. D., Mudie, S. T. & Petersen, T. C. Favored local structures in amorphous colloidal packings measured by microbeam x-ray diffraction. *Proc. Natl Acad. Sci. USA* **114**, 10344–10349 (2017).
14. Liu, A. C. Y. et al. Systematic mapping of icosahedral short-range order in a melt-spun $zr_{36}cu_{64}$ metallic glass. *Phys. Rev. Lett.* **110**, 205505 (2013).
15. Altarelli, M., Kurta, R. P. & Vartanyants, I. A. X-ray cross-correlation analysis and local symmetries of disordered systems: General theory. *Phys. Rev. B* **82**, 104207 (2010).
16. Martin, A. Orientational order of liquids and glasses via fluctuation diffraction. *IUCrJ* **4**, 24–36 (2017).
17. Darmanin, C. et al. High-throughput production and structural characterization of libraries of self-assembly lipidic cubic phase materials. *ACS Comb. Sci.* **14**, 247–252 (2012).
18. Conn, C. E. et al. High-throughput analysis of the structural evolution of the monoolein cubic phase in situ under crystallogenesis conditions. *Soft Matter* **8**, 2310–2321 (2012).
19. Cherezov, V., Fersi, H. & Caffrey, M. Crystallization screens: compatibility with the lipidic cubic phase for in meso crystallization of membrane proteins. *Biophys. J.* **81**, 225–242 (2001).
20. Cherezov, V., Clogston, J., Misquitta, Y., Abdel-Gawad, W. & Caffrey, M. Membrane protein crystallization in meso: Lipid type-tailoring of the cubic phase. *Biophys. J.* **83**, 3393–3407 (2002).
21. Duesing, R. M., Templer, R. & Seddon, J. M. Quantifying packing frustration energy in inverse lyotropic mesophases. *Langmuir* **13**, 351–359 (1997).
22. van't Hag, L., Gras, S. L., Conn, C. E. & Drummond, C. J. Lyotropic liquid crystal engineering movingbeyond binary compositional space-ordered nanostructured amphiphile self-assembly materials by design. *Chem. Soc. Rev.* **46**, 2705 (2017).
23. Parthasarathy, R. & Groves, J. T. Curvature and spatial organization in biological membranes. *Soft Matter.* **3**, 24–33 (2007).
24. SAXS Software - scatterBrain. http://archive.synchrotron.org.au/aussyncbeamlines/saxswaxs/software-saxswaxs (2019).
25. Jones, E. et al. SciPy: Open source scientific tools for Python (2001–).
26. Yoon, C. H. et al. Unsupervised classification of single-particle x-ray diffraction snapshots by spectral clustering. *Optics Express* **19**, 16542–16549 (2011).
27. Martin, A. et al. Dataset from: fluctuation x-ray diffraction reveals three-dimensional nanostructure and disorder in self-assembled lipid phases (RMIT University, Melbourne 2020).

Acknowledgements

Author contributions

A.M. and C.D. designed the experiment. B.A., A.M., C.D., T.G. and P.B. acquired funding. C.D. and F.R. prepared the samples. A.K., F.R., L.F., P.B., C.D. and A.M. collected the data with assistance from A.H. and T.R. A.K., S.S. and A.M. analysed the data. C.D., T.G., C.C. and A.M. interpreted the data and designed the geometric models. A.M. calculated many-body correlations from the geometric models. A.M. and C.D. wrote the original draft of the manuscript which was revised with input from all authors.

Competing interests

The authors declare no competing interests.

Additional information

Supplementary information is available for this paper at https://doi.org/10.1038/s43246-020-0044-z.

Correspondence and requests for materials should be addressed to A.V.M. or C.D.

Reprints and permission information is available at http://www.nature.com/reprints

Publisher's note Springer Nature remains neutral with regard to jurisdictional claims in published maps and institutional affiliations.